International Journal of Nanomedicine

Dovepress
Taylor & Francis Group

Open Access Full Text Article

ORIGINAL RESEARCH

Mitochondria-Targeting Type-I Photodynamic Therapy Based on Phenothiazine for Realizing Enhanced Immunogenic Cancer Cell Death via Mitochondrial Oxidative Stress

Zeyu Duan[1,*], Lie Li[1,*], Qiyu Zhan[1], Jian Chen[1], Qiyan Li[1], Ruiyuan Liu[1,*], Yinuo Tu[2,*]

[1]Biomaterials Research Center, School of Biomedical Engineering, Southern Medical University, Guangzhou, 510515, People's Republic of China; [2]Guangzhou Institute of Cancer Research, the Affiliated Cancer Hospital, Guangzhou Medical University, Guangzhou, Guangdong, 510095, People's Republic of China

*These authors contributed equally to this work

Correspondence: Ruiyuan Liu; Yinuo Tu, Email ruiyliu@smu.edu.cn; tuyinuo@gzhmu.edu.cn

Purpose: Photo-immunotherapy faces challenges from poor immunogenicity and low response rate due to hypoxic microenvironment. This study presents Rh-PTZ, a small organic molecule with a D-π-A structure, that simultaneously amplifies mitochondria-targeted type-I PDT-dependent immune stimulation for the treatment of hypoxic cancer.

Methods: The hydrophobic Rh-PTZ was encapsulated into F127 to prepare Rh-PTZ nanoparticles (Rh-PTZ NPs). The type-I ROS generation ability, mitochondrial targeting capacity, and ICD triggering effect mediated by Rh-PTZ NPs under LED light irradiation were investigated. Based on a 4T1 subcutaneous tumor model, the in vivo biological safety assessment, in vivo NIR fluorescent imaging, and the efficacy of PDT were assessed.

Results: Rh-PTZ could efficiently accumulate in the mitochondrial site and induce $O_2^{\bullet-}$ and •OH burst in situ under LED light irradiation, thereby causing severe mitochondrial dysfunction. Rh-PTZ can amplify mitochondrial stress-caused immunogenic cell death (ICD) to stimulate the immune response, promote the maturation of sufficient dendritic cells (DCs), enhance the infiltration of immune cells, and alleviate the tumor immunosuppressive microenvironment.

Conclusion: The mitochondria-targeting type-I PDT holds promise to enhance photo-immunotherapy for hypoxia tumor treatment and overcoming the limitations of traditional immunotherapy.

Keywords: Photo-immunotherapy, immunogenic cell death, Type-I photosensitizers, mitochondrial targeting

Introduction

Induction of immunogenic cell death (ICD) is regarded as a promising therapeutic approach for tumors due to its ability to trigger the immune response.[1–5] ICD was characterized by the release/exposure of damage-associated molecular patterns (DAMPs), which can evoke the immune system, promote the maturation of dendritic cells (DCs), stimulate the proliferation of cytotoxic T lymphocytes, and alleviate the immunosuppressive tumor microenvironment.[6,7] Unfortunately, most ICD inducers are small molecules that are toxic chemotherapy drugs. Therefore, there is an urgent need to develop a safe and effective ICD induction strategy.

Recently, photodynamic therapy (PDT) represents a promising therapeutic approach for treating cancers, wherein photosensitizers (PSs) are triggered upon light irradiation to generate cytotoxic reactive oxygen species (ROS), initiating ICD and ultimately leading to the death or necrosis of tumor cells.[8–13] Due to its characteristics of high tumor selectivity, non-invasiveness, and minimal systemic toxicity, PDT has attracted considerable attention in the treatment of tumors.[14–16] However, there are still several challenges for its clinical application. Firstly, the hypoxic tumor microenvironment (TME,

Received: 6 September 2024
Accepted: 21 December 2024
Published: 6 January 2025

pO_2 < 5 mm Hg) significantly inhibits ROS production, thereby diminishing the effectiveness of PDT to induce ICD. Recently, type-I photosensitizers, which generate $O_2^{\bullet-}$ or •OH via type-I electrons transferring process with a low O_2-dependent performance, demonstrate an exceptional capacity to overcome the constraints and display great advantage in the treatment of hypoxic tumors.[17–19] Another critical challenge facing PDT is the inherent flow of ROS, which has a very short lifespan (0.03~0.18 ms) and a small diffusion range (<20 nm).[20,21] The temporary attenuation of ROS has significantly compromised the therapeutic efficiency of PDT. Therefore, the precise accumulation of photosensitizers in subcellular organelles is crucial to improving PDT efficacy, as ROS can be fully activated for maximum cellular damage in situ. In summary, it becomes imperative to develop novel type-I photosensitizers with subcellular targeting to address these challenges.

The mitochondria, the control center of cell apoptosis and the energy house of cells, is vital for maintaining the proper function and state of cells, and its dysfunction can lead to various disorders, including cancer, aging, metabolic diseases, and degenerative diseases.[22–25] More importantly, the mitochondrion is very susceptible to ROS, making it an attractive target for organelle-targeted phototherapy.[26–29] In addition, mitochondria have been found to play a vital role in the regulation of the immune system, and tumor-associated mitochondrial antigens are potentially immunogenic. Therefore, mitochondria are suitable target to promote ICD-mediated photo-immunotherapy.[30,31] Taken together, an ideal method is to develop a mitochondria-targeting type-I photosensitizer that may efficiently trigger ICD and induce photo-immunotherapy for the treatment of hypoxic tumors.

Up to date, the small organic molecules with the electron donor-acceptor (D-A) structure were proposed to be the candidate of type-I photosensitizers due to the superior photophysical property.[32–35] For example, triphenylethylene (TPE) and diphenylamine (DPA) units were conjugated with acridinium to design the type-I photosensitizer for anticancer.[36] Our group has demonstrated rhodanine as a representative electron-deficient core could conjugate with the electron donor to develop D-A type photosensitizers.[37,38] However, to date, mitochondrial targeting type-I photosensitizer based on them has seldom been reported. Herein, we prepared a mitochondria-targeted type-I photosensitizer (Rh-PTZ) based on rhodanine to treat hypoxic cancer (Scheme 1). Rh-PTZ could accumulate in mitochondria and efficiently produce type-I ROS ($O_2^{\bullet-}$ and •OH) to induce mitochondrial dysfunction and amplify intracellular oxidative stress. In addition, mitochondria-targeted PDT triggered the release of damage-associated molecular patterns (DAMPs),

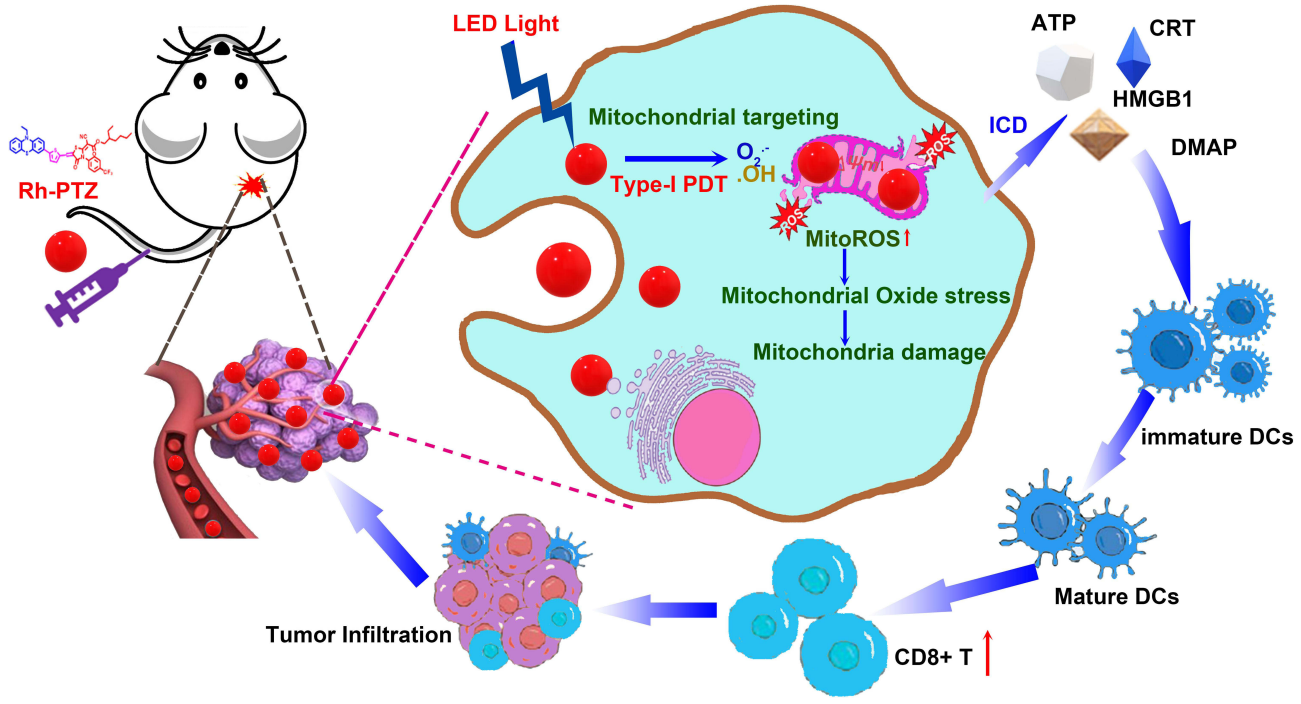

Scheme1 The schematic illustration of realizing enhanced immunogenic cell death via mitochondrial oxidative stress using Type-I photosensitizer based on rhodanine.

promoted the maturation of dendritic cells, enhanced the infiltration of CD8+ T cells, and alleviated the immunosuppressive TME. This study aims to develop type-I photosensitizers that can be applied for photoimmunotherapy of hypoxic tumors.

Materials and Methods

Characterization

NMR spectra were recorded via Bruker 400 MHz NMR with CDCl3 or DMSO-d6. UV absorption spectra were monitored on Thermofisher Evolution 300 spectropolarimeter. Fluorescent spectrum was obtained using Thermofisher Lumina spectrofluorometer. Infrared spectroscopy (IR) was recorded on a Shimadzu FTIR-8100 spectrophotometer. The ESR was recorded by Bruker ELEXSYS-II E500 CW-EPR. Cellular fluorescence images were obtained by an Olympus IX70 inverted microscope. Mass Spectrum was performed with ThermoFisher Scientific TSQ quantis LC-MS. Confocal laser scanning microscope (CLSM) images were performed on Olympus FV1000-IX81 confocal laser scanning microscope. Small animals' fluorescence imaging was carried out by Bruker FX Pro living imaging system.

Synthesis of Rhodanine

1-isothiocyanato-4-(trifluoromethyl)benzene (2.23g, 11 mmol), 2-ethylhexyl 2-cyanoacetate (1.97 g, 10 mmol), and DBU (1.52 g, 10 mmol) were added to CH_3CN (50 mL) at room temperature. After stirring for 30 min, ethyl bromoacetate (2.83 g, 17 mmol) was added to the mixture. The mixture was refluxed for 8 hours. The CH_3CN was evaporated. The solid was acidified with 1 M HCl (60 mL) and extracted with dichloromethane. The organic layer was dried over anhydrous sodium sulfate and concentrated. The crude product was purified by recrystallization in CH_3CN to yield pale yellow solid (3.56 g, 81%). ^{1}H NMR (600 MHz, $CDCl_3$) δ(ppm) 8.46~8.47 (d, J = 8.9 Hz, 2H), 7.58~7.59 (d, J = 8.8 Hz, 2H), 4.20~4.26 (m, 2H), 3.98~4.01 (m, 2H), 1.66~1.69 (m, 1H), 1.47~1.49 (t, 2H), 1.28~1.36 (m, 6H), 0.89~0.93 (m, 6H). ^{13}C NMR (300 MHz, $CDCl_3$) δ (ppm) 165.87, 165.11, 162.37, 143.95, 136.96, 130.42, 125.14, 122.96, 115.12, 68.72, 38.69, 30.21, 28.86, 23.67, 22.91, 14.04, 12.92, 11.00.

Synthesis of Rh-PTZ

5-(10-Ethyl-Phenothiazin-3-Yl)thiophene-2-Carbaldehyde Was Prepared According to the Reference[39]

5-(10-ethyl-phenothiazin-3-yl)thiophene-2-carbaldehyde (1.68 g, 5 mmol), rhodanine (2.2 g, 5 mmol), and NH_4OAc (500 mg) were added to acetic acid (30 mL). The mixture was refluxed at 90°C for 12 h under N_2 protection. After cooling the solution, the crude precipitate was filtered and washed twice with cold MeOH. The solid was recrystallized from CH_2Cl_2 (5 mL) and ethanol (50 mL) to give Rh-PTZ as a brick-red solid. Yield: 2.58 g (78%). ^{1}H NMR (600 MHz, $CDCl_3$) δ 8.04 (s, 1H), 7.86~7.87 (d, J = 8.2 Hz, 2H), 7.49~7.53 (m, 4H), 7.45 (d, J = 2.2 Hz, 1H), 7.33~7.34 (m, 1H), 7.15~7.21 (m, 2H), 6.96~6.98 (t, 1H), 6.38~6.93 (m, 2H), 4.18~4.26 (m, 2H), 3.97~4.01 (m,2H), 1.65~1.69 (m, 1H), 1.47~1.49 (m, 3H), 1.40~1.43 (m, 2H), 134~1.36 (m, 2H), 1.29~1.30 (m, 4H), 0.89~0.92 (m, 6H). ^{13}C NMR (151 MHz, $CDCl_3$) δ 166.10, 165.31, 162.64, 152.62, 145.89, 143.97, 137.56, 136.70, 135.62, 129.74, 128.89, 127.55, 127.48, 127.15, 127.06, 125.50, 125.21, 124.65, 123.89, 123.29, 122.93, 115.41, 115.26, 115.12, 112.17, 78.16, 68.53, 42.10, 38.70, 30.18, 28.90, 23.63, 22.91, 14.05, 12.92, 11.00. ESI-HRMS m/z: calcd. for $C_{40}H_{37}F_3N_3O_3S_3^+$ $[M-H]^+$ 760.1944, found: 760.1948.

Preparation of Rh-PTZ Nanoparticles

Rh-PTZ nanoparticles were prepared by a well-established nanoprecipitation method. Rh-PTZ (1 mg) and F127 (4 mg) were dissolved into 1 mL of THF and mixed homogeneously. The mixed solution was injected once into 9 mL of double distilled water under ultrasonic conditions for 5 min, then transferred to a dialysis bag (MWCO = 3600) and dialyzed against deionized water for 24 h. The Rh-PTZ nanoparticles were concentrated and calibrated before use. The concentration of Rh-PTZ in Rh-PTZ Nanoparticles was determined by standard curve method. $Y(A_{510nm})$ = 0.03179X (M)-0.02689 (R=0.99956).

 https://doi.org/10.2147/IJN.S494970

DFT Calculations

The molecular geometries were optimized by Gaussian 09[1] on the calculation level of B3LYP/6-311G(d) under normal convergence criteria with consideration of water solvent environment. The electron cloud distribution and energy calculations were predicted using B3LYP/6-311G(d) based on the optimized structure.

The Detection of Singlet Oxygen Generated from Rh-PTZ via ABDA

9.10-Anthracenediyl-bis(methylene)-dimalonic acid (ABDA) is used to monitor $^1O_2$ production. The concentrations of ABDA and Rh-PTZ in their aqueous mixture were 100 μM and 10 μM, respectively. The above solution is irradiated with an LED white light (80 mW/cm^2) for different periods of time. The change in the absorption signal of the indicator ABDA at 380 nm was monitored by an ultraviolet-visible spectrometer to monitor the generation of $^1O_2$.

The Detection of ROS Generated from Rh-PTZ via DCFH

2',7'-Dichlorodihydrofluorescein (DCFH), which was obtained from 2',7'-dichlorodihydrofluorescein diacetate (DCFH-DA), was used as the probe to evaluate ROS generation. The concentrations of DCFH and Rh-PTZ in their aqueous mixture were 10 μM and 10 μM, respectively. The above solution is irradiated with an LED white light (80 mW/cm^2) for different periods of time. The change in the fluorescence signal of DCFH is monitored by a fluorescence spectrometer. The excitation wavelength is 480 nm, and the fluorescence intensity of DCFH at 525 nm is recorded to indicate ROS generation.

The Detection of Superoxide Anion Radical ($O_2^{\bullet-}$) Generated from Rh-PTZ via DHR123

Dihydrorhodamine 123 (DHR123) is used as an indicator of $O_2^{\bullet-}$, which can be converted to rhodamine 123 in the presence of $O_2^{\bullet-}$. The concentrations of DHR123 and Rh-PTZ in their aqueous mixture were 10 μM and 10 μM, respectively. The above solution is irradiated with an LED white light (80 mW/cm^2) for different periods of time. The change in the fluorescence signal of DHR123 is monitored by a fluorescence spectrometer. The excitation wavelength used is 480 nm, and the fluorescence intensity of DHR123 at 525 nm is recorded to indicate superoxide anion radical generation.

The Detection of Hydroxyl Radical (•OH) Generated from Rh-PTZ via TMB

3.3',5,5'-Tetramethylbenzidine dihydrochloride (TMB) is used to monitor •OH production. The concentrations of TMB and Rh-PTZ in their aqueous mixture were 10 mM and 10 μM, respectively. The above solution is irradiated with an LED white light (80 mW/cm^2) for different periods of time. The change in the UV absorption signal of TMB-OX is monitored by a UV-vis spectrometer. The change in the absorption signal of TMB-OX at 450 nm was monitored by an ultraviolet-visible spectrometer to monitor the generation of •OH.

The Detection of Hydroxyl Radical (•OH) Generated from Rh-PTZ via HPF

Hydroxyphenyl fluorescein (HPF) is used to monitor •OH production. The concentrations of HPF and Rh-PTZ in their aqueous mixture were 5 μM and 10 μM, respectively. The change in the fluorescence signal of HPF is monitored by a fluorescence spectrometer. The excitation wavelength used is 480 nm, and the fluorescence intensity of HPF at 520 nm is recorded to indicate •OH generation.

ROS Generated from PDT Detection with Electron Paramagnetic Resonance (EPR)

DMPO was used as a trapping agent for •OH and $O_2^{\bullet-}$. The Rh-PTZ was respectively dissolved in H_2O/DMSO (V_{water}/V_{DMSO} = 99:1) mixed solution. Trapping agents were dissolved in CH_3OH, which was further added into Rh-PTZ aqueous solution to reach a final concentration of 100 μM and 10 μM for trapping agent and Rh-PTZ, respectively. The EPR spectra of the mixtures were recorded before and after light irradiation (LED white light, 10 min, 80 mW/cm^2). The electron paramagnetic resonance (EPR, Bruker A300) spectra were measured to evaluate ROS generation. For comparison, an electron paramagnetic resonance spectrometer tested the DMPO + Rh-PTZ (10 μM) group.

Cell Culture

4T1 cells were provided from the Beyotime Co. Ltd. 4T1 cells were maintained as monolayer cultures in DMEM at 37°C in an CO_2 incubator (5% CO_2), the mediums were supplemented with 10% FBS and 1% penicillin/streptomycin. The cells were cultured until confluence was reached before each experiment.

Intracellular ROS Detection

For the total ROS detection, 4T1 cells were incubated with 10 μM of Rh-PTZ for 4 h followed by incubation with 10 μM DCFH-DA for 30 min. Cells were irradiated with white light (80 mW/cm^2) for 10 min. The post-treatment cells were then imaged by CLSM with excitation filter of 488 nm, and emission filter of 500–530 nm. For comparison, PBS group and Rh-PTZ (10 μM) group were tested.

For $O_2^{\bullet-}$ detection, 4T1 cells were incubated with 10 μM of Rh-PTZ for 4 h, followed by incubation with 10 μM DHR123 for another 30 min. Cells were irradiated with white light (80 mW/cm^2) for 10 min. Then the cells were immediately observed using CLSM with the excitation wavelength of 488 nm, and emission collection wavelength from 500 nm to 550 nm. For comparison, PBS group and Rh-PTZ (10 μM) group were tested.

For •OH detection, 4T1 cells were incubated with 10 μM of Rh-PTZ for 4 h, followed by incubation with 5 μM HPF for another 30 min. Cells were irradiated with white light (80 mW/cm^2) for 10 min. Then the cells were immediately observed using CLSM with the excitation wavelength of 488 nm, and emission collection wavelength from 500 nm to 550 nm. For comparison, PBS group and Rh-PTZ (10 μM) were tested.

Colocalization Experiments

4T1 cells were incubated with Rh-PTZ (10 μM) in culture medium for 4 h at 37°C, and then the cells were washed with PBS three times. Mito-Tracker Green or Lyoso-tracker Green was added, and co-incubated for another 30 min and cell imaging was then carried out after washing cells with PBS three times. Rh-PTZ was collected 660~720 nm (λ_{ex} = 500 nm) for near infrared region, which was marked with red color. Emission from Mito-Tracker Green or Lyoso-tracker Green was collected based on the manufacturer's instruction.

Confocal Imaging of Rh-PTZ

4T1 cancer cells were cultured in a 20 mm glass bottom petri dish at 37°C in a humidified environment containing 5% CO_2. After the cells grew to 70% confluence, culture medium was aspirated and the cells were washed with PBS for three times. 10 μM Rh-PTZ containing DMEM (10% FBS) was then added to cell culture petri dish. After 6 h incubation, the culture medium was aspirated and the cells were washed with PBS for three times. The cells were fixed with 4% paraformaldehyde at room temperature for 15 min, then washed with PBS 3 times and incubated with 1 μg/mL DAPI containing DMEM for 30 min. CLSM images were acquired after washing the cells with PBS buffer for three times.

Cytotoxicity Evaluated by CCK-8 Assay

To detect the dark cytotoxicity, 4T1 cells were seeded in 96-well plates and pre-cultured for 24 h, and then the medium was replaced by Rh-PTZ NPs solution with Rh-PTZ concentration equivalent to 0, 1, 2, 4, 6, 8, 10, 12 μM. After a 4 h incubation, the cells were gently washed by PBS buffer for three times to remove the non-internalized nanoparticles, thereafter, the cells were cultured for another 24 h (37°C, 5% CO_2). The cell viabilities were determined by CCK-8 kit, and the results were presented as average ± SD (n = 5).

In vitro Toxicity Evaluation

4T1 cells were seeded in 96-well plates and pre-cultured for 24 h, and then the medium was replaced by Rh-PTZ NPs PBS solution at appropriate concentrations for 2 h, and then washed with phosphate buffer saline (PBS). Cells were irradiated with white light (80 mW/cm^2) for 10 min. After treatment, the cells (100 μL) were seeded on a 96-well plate and incubated overnight at 37°C under 5% CO_2. The CCK-8 kit then determined the cell viability. The absorbance at 450 nm was recorded on a microplate reader. The cells incubated with PBS or Rh-PTZ NPs were set as control group.

Immunofluorescence Analysis

4T1 cells were seeded in 6-well plates (2×10^5 cells/well) for 12 h. After that, the cells were treated with 10 μM of Rh-PTZ for 4 h. Then, the cells in irradiation groups were exposed to white light (80 mW/cm^2) for 10 min. After further incubation for 24 h, the cells were washed twice with PBS and fixed with 4% paraformaldehyde at room temperature for 15 min, then washed with PBS 3 times. 0.3% Triton X-100 was added for 10 min and the cells were washed with PBS 3

times. After cells were blocked with 5% BSA at room temperature for 1 h, antibodies were added for incubation at 4°C overnight. After cells were washed three times with PBS, the secondary antibodies were applied at room temperature for 1 h in dark. After staining with DAPI, the cells were observed under CLSM.

Cellular Adenosine Triphosphate (ATP) Detection

4T1 cells were seeded in 6-well plates (2×10^5 cells/well) for 12 h. After that, the cells were treated with 10 μM of Rh-PTZ for 4 h. Then, the cells in irradiation groups were exposed to white light (80 mW/cm^2) for 10 min. After further incubation for 24 h, the cells were collected to detect the intracellular ATP concentrations by the ATP assay Kit, and the results were normalized by protein concentrations measured by BCA.

Examination of ICD Biomarkers

4T1 cells were seeded in 6-well plates (2×10^5 cells/well) for 12 h. After that, the cells were treated with 10 μM of Rh-PTZ for 4 h. Then, the cells in irradiation groups were exposed to white light (80 mW/cm^2) for 10 min. The cells with non-irradiation were set as controls. Then, the cells were incubated for another 24 h before detecting surface-exposed CRT and intracellular HMGB1 by CLSM according to the protocol of immunofluorescence analysis. Further, the released HMGB1and ATP in the medium was determined by the ELISA assay kit.

Examination of Cytokines

4T1 cells were seeded in 6-well plates (2×10^5 cells/well) for 12 h. After that, the cells were treated with 10 μM of Rh-PTZ for 4 h. Then, the cells in irradiation groups were exposed to white light (80 mW/cm^2) for 10 min. The cells with non-irradiation were set as controls. The ELISA assay kit determined the released TNF and IL-6 in the medium.

Construction of Tumor Models

Five weeks old female BALB/c mice were provided by the Animal Center of Southern Medical University. All animal experiments were carried out under the guidance of the protocols approved by the local Ethical Committee in compliance with the Chinese law on experimental animals and followed regulations of the Institutional Animal Care and Use Committee of South Medical University (SCXK 2016–0041). All mice were kept in SPF-level feeding conditions with adequate water and food. The temperature is kept at 26°C, the humidity is 50% and a 12 h light/dark cycle.

In vitro NIR Fluorescence Imaging of Rh-PTZ

The tumor-bearing mouse was anesthetized with isoflurane to remove fur. Next, the aqueous solution (100 μL) of Rh-PTZ (100 μM) was intravenously injected into the mouse. After injection, the mouse was imaged with the small animal imaging system at designated time points.

In vivo Antitumor Activity

The abscopal effect was investigated in the bilateral tumor model. 4T1 cells (8×10^5) were subcutaneously injected into the left flank of female BALB/c mice as the primary tumors. 6 days later, the mice were subcutaneously injected with 4T1 cells (4×10^5) again into the right flank as the abscopal tumors. When tumors grew to approximately 100 mm^3, randomly assigned mice were treated with (1) control (PBS intravenously injection), (2) Rh-PTZ (intravenously injection), (3) Rh-PTZ NPs (intravenously injection), (4) Rh-PTZ (intravenously injection) + Light (LED white light irradiation).

Each group contained five mice, and 100 mL of Rh-PTZ (100 μM) were intravenously injected. The tumors were subjected to white light irradiation for 5 min at a power density of 80 mW/cm^2 at 24 h after the Rh-PTZ injection while the distant tumors were without irradiation. 24 h after different treatments, one mouse in each group was sacrificed by cervical dislocation for necropsy, and its tumor was collected for tissue slicing, staining, and the investigation of immune response. For the left mice, their body weights and tumor sizes were measured every 2 days for a period of 14 days, and the tumor volumes were calculated using the following formula: Volume = (Length×Width^2)/2 (length (L) is the longest diameter and width (W) is the shortest diameter perpendicular to length).

Flow Cytometry Analysis

After the 24 hour treatment, the mice in group 5 were sacrificed by cervical dislocation. The tumor from treated mice were harvested and digested at 37°C in buffer containing 1 mg/mL collagenase I and 200 mg/mL DNase I for 30 min. Subsequently, the mixture was gently ground and filtered to collect individual cells. Antibodies used to stain different immune cells were as follows (all antibodies from Abcam technology Co., Ltd): PE Anti-CD86 antibody (ab275357), PE/Cy Anti-CD80 antibody (ab234229), PE-Cy Anti-CD4 antibody (ab233660), APC Anti-CD8 antibody (ab313759), PE-Cy Anti-Ly-6C (Gr-1) antibody (ab25572), APC Anti-CD11b antibody (ab25482), PE Anti-F4/80 antibody (ab105156). Flow cytometry data were acquired on flow cytometer (LSR Fortessa, BD Biosciences) and analyzed by FlowJo software (TreeStar, version 10.8).

Histological Analysis

After the 24-hour treatment, the mice in group 5 were sacrificed by cervical dislocation for necropsy, their major organs including hearts, livers, spleens, lungs, and kidneys were harvested for tissue slicing and staining with hematoxylin and eosin (H&E) and TUNEL labeling and assess via optical microscopy.

The Serum Biochemical Data

For the blood routine test, the blood of healthy mice and the tumor-bear mice after different treatments were collected, and then blood routine test was conducted on the automatic hematology analyzer.

Statistical Analysis

Unpaired two-tailed Student's *t*-test was used to compare the statistical significance between two data groups. One-way analysis of variance (ANOVA) with a Bonferroni post hoc test was used to compare three or more groups. Quantitative data were indicated as mean ± S.D. Asterisks were used to represent significant differences (n.s.: no significance, $*P < 0.05$). The statistical analysis was performed by using GraphPad Prism 8.0 software.

Result and Discussion

The Preparation and Optical Property of Rh-PTZ

The compound Rh-PTZ was fabricated based on a typical D-A configuration with intramolecular charge transfer (ICT) properties. Phenothiazine was employed as the D moiety due to its strong electron-donating ability, efficient charge transfer properties, and high photostability. The thiophene group was utilized as a-bridge to extend the conjugation and improve the electron-donating ability. In addition, the rhodanine moiety served the function of the A part to facilitate triplet sensitization. The synthetic routes for Rh-PTZ are exhibited in Scheme S1, with the final product being easily synthesized via Knoevenagel condensation reactions. The molecular structure of Rh-PTZ was confirmed by nuclear magnetic resonance (NMR) and high resolution mass spectrometry (HRMS) (Figure S1-S5).

To enhance the biocompatibility and biostability, the hydrophobic Rh-PTZ was encapsulated into F127 (polyethylene-polypropylene glycol) to prepare Rh-PTZ nanoparticles (Figure 1A). As illustrated in Figure 1B, the transmission electron microscope (TEM) image exhibited that the Rh-PTZ nanoparticles exhibited a particle size of 90 nm. As evidenced by the dynamic light scattering (DLS) analysis, the hydrated particle size of Rh-PTZ nanoparticles was determined to be 100 nm (Figure 1C). Furthermore, the particle size stability of Rh-PTZ nanoparticles at different time points was evaluated using dynamic light scattering (DLS). The size of Rh-PTZ nanoparticles remained relatively stable over a two-week period in serum (Figure S6), which indicated that they could be further applied in vivo. The photophysical characteristics of Rh-PTZ were investigated through UV-vis absorption and fluorescence spectroscopy. As illustrated in Figure 1D, the absorption and emission spectra of Rh-PTZ Nanoparticles exhibited an absorption peak at approximately 510 nm and a fluorescent emission peak at 685 nm. To evaluate the photostability of Rh-PTZ, we have investigated the PL intensity and absorbance under LED light irradiation. The absorbance of Rh-PTZ exhibited slight alteration after LED light irradiation (Figure S7). Furthermore, as demonstrated in Figure S8, the PL intensity of Rh-PTZ

 https://doi.org/10.2147/IJN.S494970

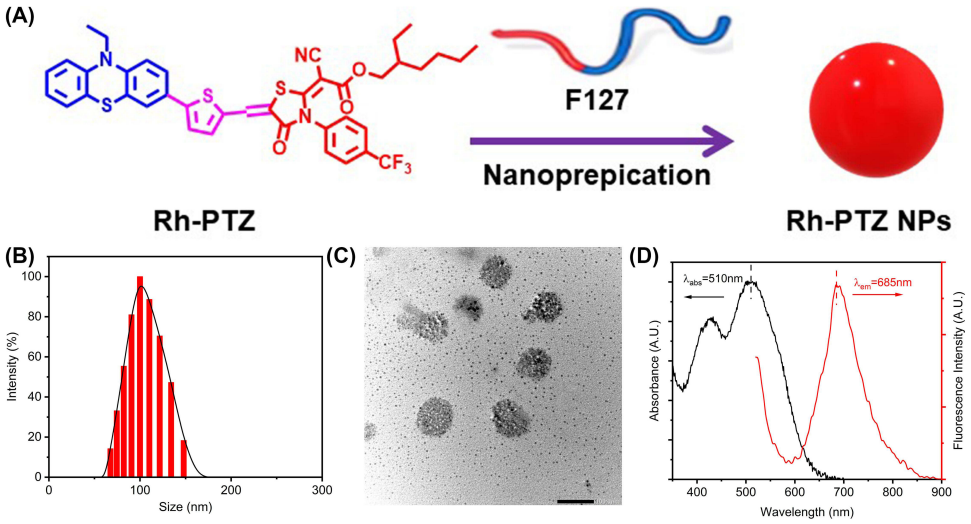

Figure 1 The preparation and optical properties of Rh-PTZ. (**A**) The scheme description of Rh-PTZ nanoparticles. (**B**) The TEM imaging of Rh-PTZ nanoparticles. (**C**) The DLS of Rh-PTZ nanoparticles. (**D**) The UV-vis and fluorescent spectrum of Rh-PTZ.

exhibited 91% retention of its initial value after irradiation. These findings substantiate the suitability of Rh-PTZ for PDT.

The Type-I Photodynamic Effect of Rh-PTZ

To investigate the photodynamic properties, the total ROS-producing abilities of Rh-PTZ were examined using 2.7-dichlorodihydrofluorescein (DCFH) as an indicator under white light irradiation. As illustrated in Figure 2A, Figure S9 and Figure S10, the fluorescence intensity of DCFH exhibited a rapid increase in the presence of Rh-PTZ under continuous irradiation, whereas slightly enhancement in fluorescence intensity was observed for the irradiated solution containing DCFH alone.

In addition, dihydrorhodamine 123 (DHR123), a superoxide anion radical probe, was employed to investigate $O_2^{\bullet-}$ production ability of Rh-PTZ. As indicated in Figure 2B and Figure S11, the PL intensity of DHR 123 after 60 s white light irradiation was over 15.8-fold of that before the irradiation, implying the generation of $O_2^{\bullet-}$. Furthermore, the •OH production efficiency of Rh-PTZ was measured by utilizing hydroxyphenyl fluorescein (HPF) as an indicator. The fluorescent intensity of HPF enhanced more than 23.6-fold under continuous irradiation for 60 s in the presence of Rh-PTZ, further confirming that Rh-PTZ could produce •OH efficiently through type-I PDT process (Figures 2C and S12). The same conclusions were drawn when TMB was utilized to monitor •OH generation (Figures 2D and S13).

Moreover, we later used 9.10-anthracenediylbis(methylene)-dimalonic acid (ABDA) as $^1O_2$ indicator for Rh-PTZ. As demonstrated in Figure 2E, the absorbance of ABDA only attenuates by 0.18% after 60 s irradiation. The observations show that Rh-PTZ is difficult to produce $^1O_2$ via type-II energy transfer process.

Considering the particular benefit of type-I photosensitizer for PDT in the hypoxic environment, the photodynamic performance of Rh-PTZ under such conditions is further explored. DHR123 and HPF steadily increase their fluorescence under LED light irradiation (Figures S14 and S15), which is attributable to the unaltered production of $O_2^{\bullet-}$ and •OH. This shows that the photosensitization process of Rh-PTZ is an O_2-insensitive process.

To further confirm the production of type-I ROS ($O_2^{\bullet-}$ and •OH), 5.5-dimethyl-1-pyrroline-N-oxide (DMPO) was selected as the spin-trap indicator to carry out electron spin resonance (ESR) investigation. In the presence of DMPO and Rh-PTZ, a typical four-line ESR signal with 1:2:2:1 intensity under LED white light irradiation was detected, that is the characteristic resonances for DMPO/•OH adduct. In addition, an obvious six-line resonance with 1:2:1:2:1:2 was also observed, derived from DMPO/ $O_2^{\bullet-}$ adduct (Figure 2F). These findings suggest that Rh-PTZ may produce cytotoxic $O_2^{\bullet-}$ and •OH through type-I photodynamic process upon LED white light radiation (Figure 2H), indicating its potential as a type-I photosensitizer for phototheranostics in biomedical applications.

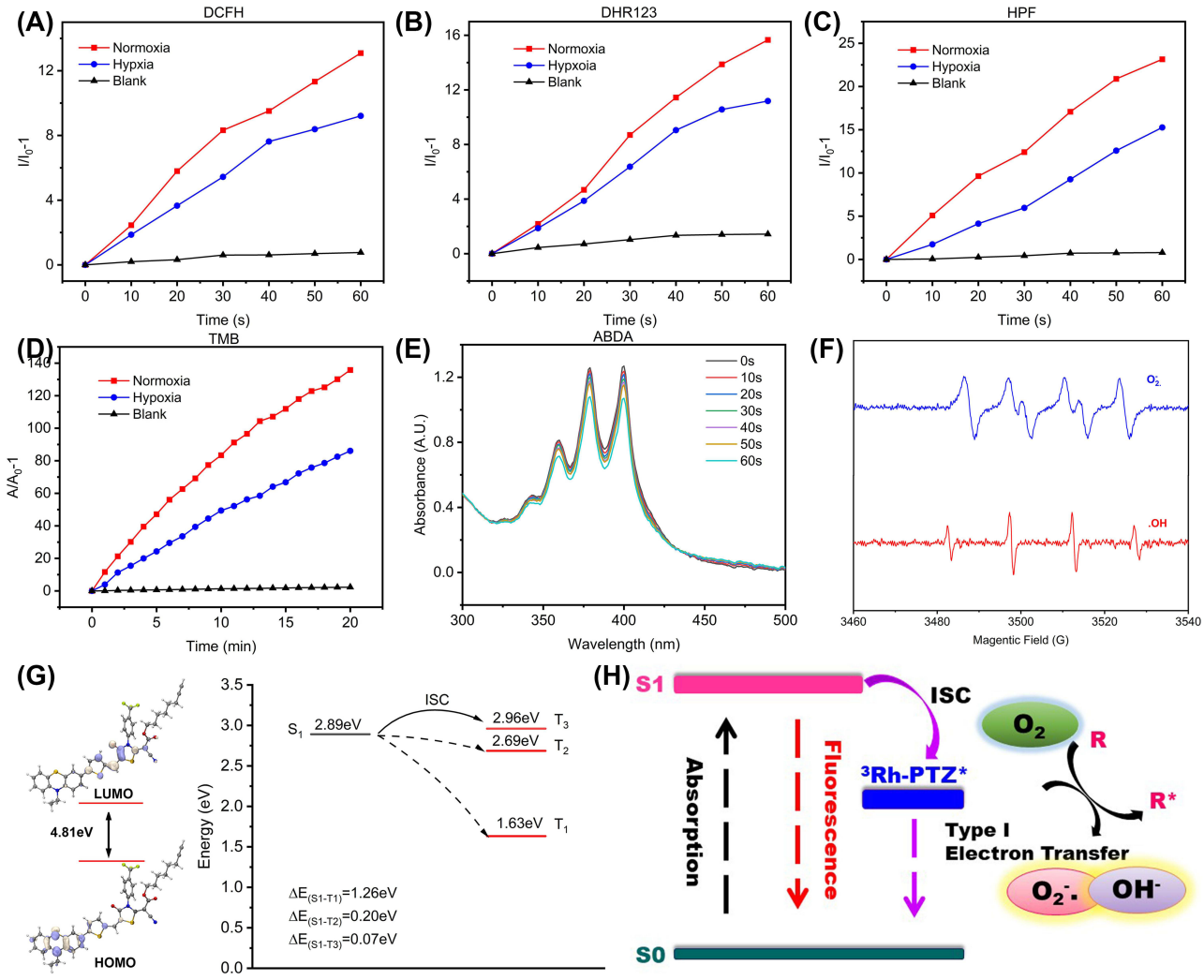

Figure 2 The type I photodynamic therapy of Rh-PTZ. (**A**) Fluorescence enhancement of DCFH (10 (**M**) at 525 nm in the presence of Rh-PTZ (10 (**M**) under LED light irradiation (80 mW/cm^2). (**B**) Fluorescence enhancement of DHR123 (10 (**M**) at 520 nm in the presence of Rh-PTZ (10 (**M**) under LED light irradiation (80 mW/cm^2). (**C**) Fluorescence enhancement of HPF (5 (**M**) at 520 nm in the presence of Rh-PTZ (10 (**M**) under LED light irradiation (80 mW/cm^2) under normoxia or hypoxia conditions. (**D**) Absorption increases of TMB (10 mM) at 425 nm in the presence of Rh-PTZ (10 (**M**) under LED light irradiation (80 mW/cm^2). (**E**) The absorption of ABDA for $^1O_2$ detection. (**F**) EPR spectra of $O_2^{\bullet-}$ and •OH generation from Rh-PTZ under LED light irradiation (80 mW/cm^2). (**G**) Calculated HOMO and LUMO, Excitation energies of the low-lying excited states between them based on the optimized S_0-geometries of Rh-PTZ. (**H**) Illustration of $O_2^{\bullet-}$ and •OH generation of Rh-PTZ via type-I process.

To elucidate the underlying mechanism of the photochemical property of Rh-PTZ, we perform density functional theory (DFT) calculation to gain insight into the electronic nature of Rh-PTZ. Rh-PTZ displays local excitation (LE) character to the same extent and obtains the absolute orbital overlap HOMO-LUMO of 4.81 eV (Figure 2G). The excited states nature of Rh-PTZ is additionally calculated with time-dependent density functional theory (TD-DFT). The energy of S_1 and T_1 are estimated to be 2.89 eV and 1.63 eV. Such large $\Delta E_{S1\text{-}T1}$ of 1.26 eV generally denotes a low intersystem crossing (ISC) efficiency, thus rendering Rh-PTZ ineligible to generate $^1O_2$ utilizing type-II energy transfer process to surrounding oxygen. This is because the ISC rate is inversely proportional to $\Delta E_{S1\text{-}T1}$. The energy gap ($\Delta E_{S1\text{-}Tn}$) below 0.3 eV is a decisive factor for an efficient ISC process.[40] The energy gap between S_1 and the nearest T_2 ($\Delta E_{S1\text{-}T2}$ = 0.02eV) is less than 0.3 eV, and this quite small energy gap could induce the ISC process to occur from S_1 to T_2 for Rh-PTZ effortlessly. Moreover, the additional ISC channel between S_1 and T_3 is accessible due to its $\Delta E_{S1\text{-}T3}$ value.

https://doi.org/10.2147/IJN.S494970

In vitro Mitochondrial Oxidative Stress and ICD Effect Induced by Type-I PDT Based on Rh-PTZ

Inspired by the ROS production of Rh-PTZ in vitro, we wondered about the subcellular distribution of Rh-PTZ. The intracellular distribution of Rh-PTZ was examined using commercially available organelle-selective trackers (Figure 3A and B). Compared to

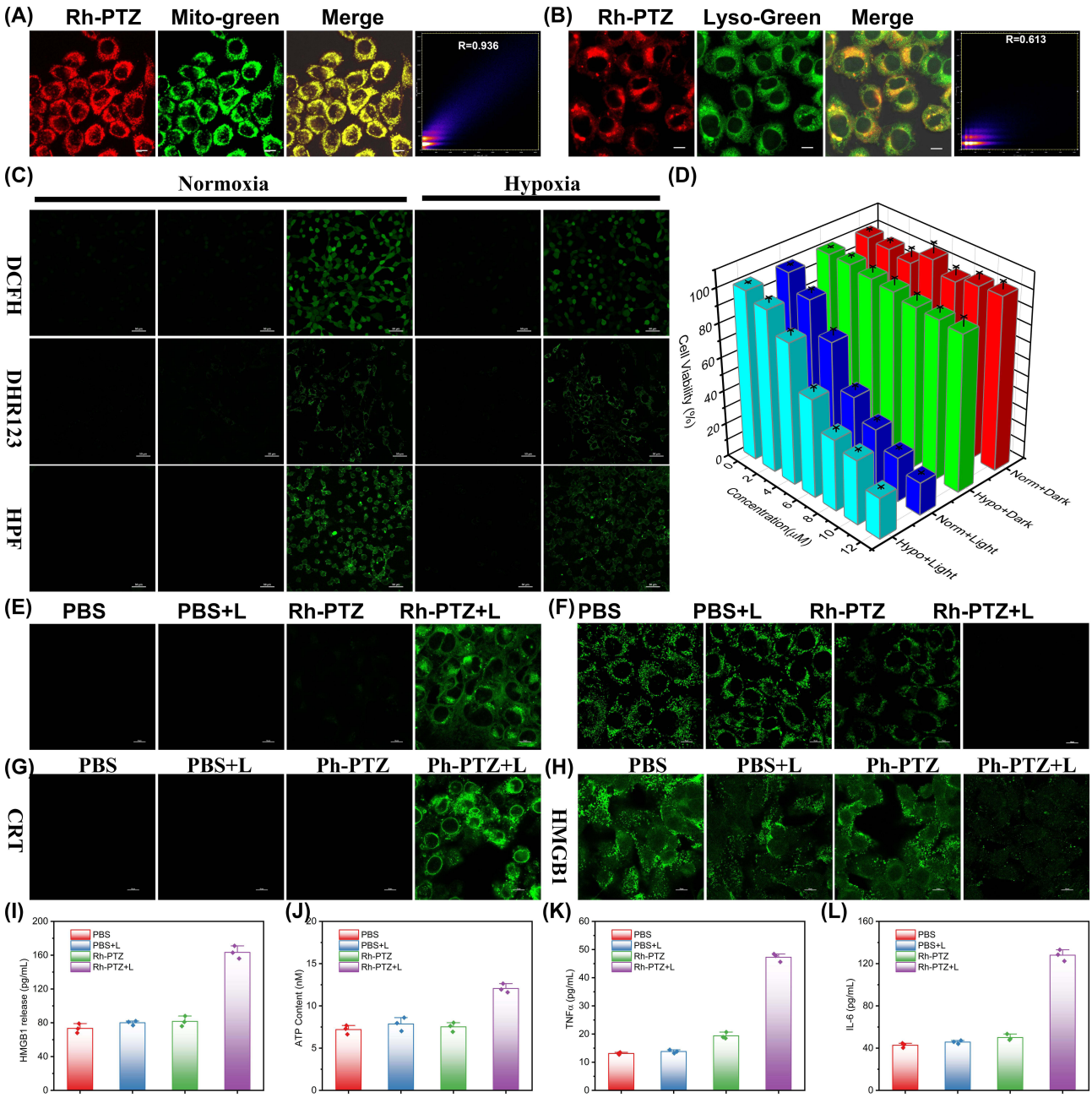

Figure 3 The type-I photodynamic therapy and ICD triggering in vitro. (**A**) The colocation of Rh-PTZ (in red) with Mito-tracker green (in green) in 4T1 cells, the scale bar = 10 M. (**B**) The colocation of Rh-PTZNPs (in red) with Lysos-tracker green (in green) in 4T1 cells, the scale bar = 10 M. (**C**) ROS detection in 4T1 cells under normoxia and hypoxia conditions using DCFH-DA, DHR123, and HFP, as total ROS, $O_2^{\bullet-}$, and •OH fluorescence indicators, respectively, the scale bar = 10 M. (**D**) Cytotoxicity of Rh-PTZ NPs in the dark and under Light irradiation (80 mW/cm^2, 10 min) on 4T1 cells under normoxia or hypoxia. (**E**) CLSM images of MitoROS generated in 4T1 cells after different treatments, the scale bar = 10 M. (**F**) CLSM images of mitochondrial membrane potential using Rhod123 as an indicator in 4T1 cells after different treatments, the scale bar = 10M. (**G and H**) Representative CLSM images of 4T1cells treated with various treatments anti-HMGB1 antibodies and anti-CRT, respectively, the scale bar = 10M. (**I**) The HMGB1 was released in the supernatant of 4T1 cells after different treatments. (**J**) The ATP in the supernatant of 4T1 after different treatments. (**K**) TNF and (**L**) IL-6 levels in the supernatant of 4T1 after different treatments.

https://doi.org/10.2147/IJN.S494970

other probes, the NIR fluorescence of Rh-PTZ overlapped well with the green fluorescence of Mito-tracker green (Pearson's coefficient: 0.91), confirming that Rh-PTZ was enriched in mitochondria.

Encouraged by the efficient type-I ROS production capacity of Rh-PTZ, we proceeded to study the PDT performance of Rh-PTZ in vitro under normoxic or hypoxic settings (Figure 3C). Under both normoxic and hypoxic conditions, the intracellular ROS generation of Rh-PTZ in 4T1 cells was measured using three different fluorescent probes. 2-7-Dichlorodihydrofluorescein diacetate (DCFH-DA) was selected to investigate total ROS. Moreover, DHR123 and HPF were selective probes for $O_2^{\bullet}-$, and •OH, respectively. 4T1 cells were treated with Rh-PTZ (10 M) and various markers, then irradiated under LED white light (80 mW/cm^2, 10 min), and eventually carried out to CLSM imaging. All three indicators demonstrated bright green fluorescence under normoxic conditions, confirming that •OH and $O_2^{\bullet}-$ were generated. Moreover, three probes also exhibited green fluorescence even under hypoxic environment. However, no ROS species were detected without LED white light irradiation even under normoxic circumstances. All these data revealed that Rh-PTZ could produce $O_2^{\bullet}-$ and •OH via the type-I process for the treatment of hypoxia tumors.

Moreover, the in vitro cytotoxicity of Rh-PTZ in normoxic or hypoxic circumstances was studied using the CCK8 assay. As demonstrated in Figure 3D, the vitality of 4T1 cells was >93% in both the normoxic and hypoxic conditions without irradiation. Conversely, following irradiation (LED, 80 mW/cm,^{2} 10 min), the viability of 4T1 cells dropped to <18% and <24% in the normoxic and hypoxic cells, respectively.

Due to the mitochondria targeting type-I PDT effect of Rh-PTZ, we wondered whether Rh-PTZ could boost mitochondrial oxidative stress to induce mitochondria damage. Mitochondrial superoxide probes (MitoSOX) were employed to measure ROS generation in mitochondria following various treatments. As demonstrated in Figure 3E, the 4T1 cells in the Rh-PTZ + Light group exhibited the highest fluorescence intensity in mitochondria, indicating the largest ROS formation in mitochondria of 4T1 cells following PDT treatment. Hence, Rh-PTZ can directly assault the mitochondria, leading to a domino effect of mitochondrial ROS burst that induces mitochondrial stress. In addition, to evaluate the mitochondrial damaging effect of Rh-PTZ, Rhod 123 was selected as an indicator to investigate the mitochondrial membrane potential (MMP) level of 4T1 cells. As shown in Figure 3F, the green fluorescence from Rhod 123 was drastically quenched in the 4T1 cells incubation with Rh-PTZ upon LED white light irradiation, verifying the depolarization of MMP and mitochondrial damage.

The above studies confirmed that Rh-PTZ + L could rapidly produce large amounts of type-I ROS in situ to trigger the mitochondrial oxidative stress, which could induce ICD and the release of a series of damage-associated molecular patterns (DAMPs) such as Calreticulin (CRT), high mobility group box B1 (HMGB1), and adenosine triphosphate (ATP). These markers were monitored in 4T1 cells to validate the ICD effect of tumor cells. Under light irradiation, 4T1 cells that were stained with Rh-PTZ greatly increased the accumulation of CRT on the cell membrane (Figure 3G). Moreover, after mitochondria-targeted PDT, HMGB1 released from the nucleus was considerably enhanced (Figure 3H and I). Besides, the amount of ATP in 4T1 cell cultures after different treatments was studied using an ATP assay kit. As shown in Figure 3J, 4T1 cells treated with Rh-PTZ +L produced more ATP than other groups, demonstrating that mitochondria-targeted PDT might greatly improve extracellular ATP expression. These data revealed that mitochondria-targeted PDT effectively triggered ICD and induced adaptive immune responses.

Furthermore, the expression levels of cytokines including TNFα and interleukin-6 (IL-6) in the cell culture supernatant were investigated by enzyme-linked immunosorbent assay (ELISA) kits (Figure 3K and L). The highest secretion levels of TNFα and interleukin-6 (IL-6) were reported after Rh-PTZ + L treatment, indicating that the Rh-PTZ + L might contribute to the activation of ICD in 4T1 cells.

The in vivo Imaging

The distribution behavior of Rh-PTZ was evaluated following intravenous administration. Rh-PTZ was administered intravenously into 4T1 tumor-bearing mice through the tail vein, and the animals were then imaged using IVIS at various time points post-injection. The amount of fluorescence in Rh-PTZ-treated tumors increased significantly and peaked around 24 h after intravenous injection (Figure S16). Therefore, PDT was performed at 24 h post-administration. More importantly, even at 72 hours after the intravenous injection, the NIR fluorescence was still observed at the tumor site, indicating exceptional intratumorally retention. In addition, the major organs (heart, liver, spleen, lung, and kidney) and

tumors of the mice were dissected for ex vivo fluorescence imaging. The fluorescence images showed that Rh-PTZ may enhance intratumorally accumulation, which is necessary for therapeutic efficacy (Figure S17).

Therapeutic Effects in vivo

Inspired by the high biocompatibility and tumor accumulation capacity, we subsequently investigated the anticancer efficiency of mitochondria-targeted PDT in the 4T1 tumor model. When the tumor volume reached approximately 200 mm^3, mice were randomly assigned to 4 groups (n = 4 per group) and intravenously injected with PBS or Rh-PTZ. At 24 hours after injection, white light laser (80 mW/cm^2) stimulation was delivered to both irradiation groups for 10 minutes (Figure 4A). Rh-PTZ +L group exhibited the highest tumor inhibition rate according to the data (Figure 4B and C). The mice were entirely sacrificed on the fourteenth day, and the tumors were collected. The Rh-PTZ +L-treated animals exhibited the least tumors (Figure 4D). In addition, Rh-PTZ + L-treated mice demonstrated the smallest tumor weight, which was only 5.4% of that of PBS-treated mice, according to the results of the tumor weighting (Figure 4E). Throughout the therapy time, neither group's body weights of mice were reduced (Figure 4F). All of these data confirmed the outstanding PDT performance of Rh-PTZ.

The ROS levels in tumor tissues were subsequently examined using immunofluorescence labeling. The ROS production in tumor tissues after various therapies was detected by DCFH-DA on day 2. Green DCF fluorescence was observed in tumors of Rh-PTZ +L group, suggestive of a robust PDT effect mediated by the Rh-PTZ (Figure S18).

To determine the amount of apoptosis and necrosis in tumor tissues following different treatments, H&E staining and TUNEL staining were carried out. Histological examination revealed that the PBS group exhibited severe histological damage to tumor

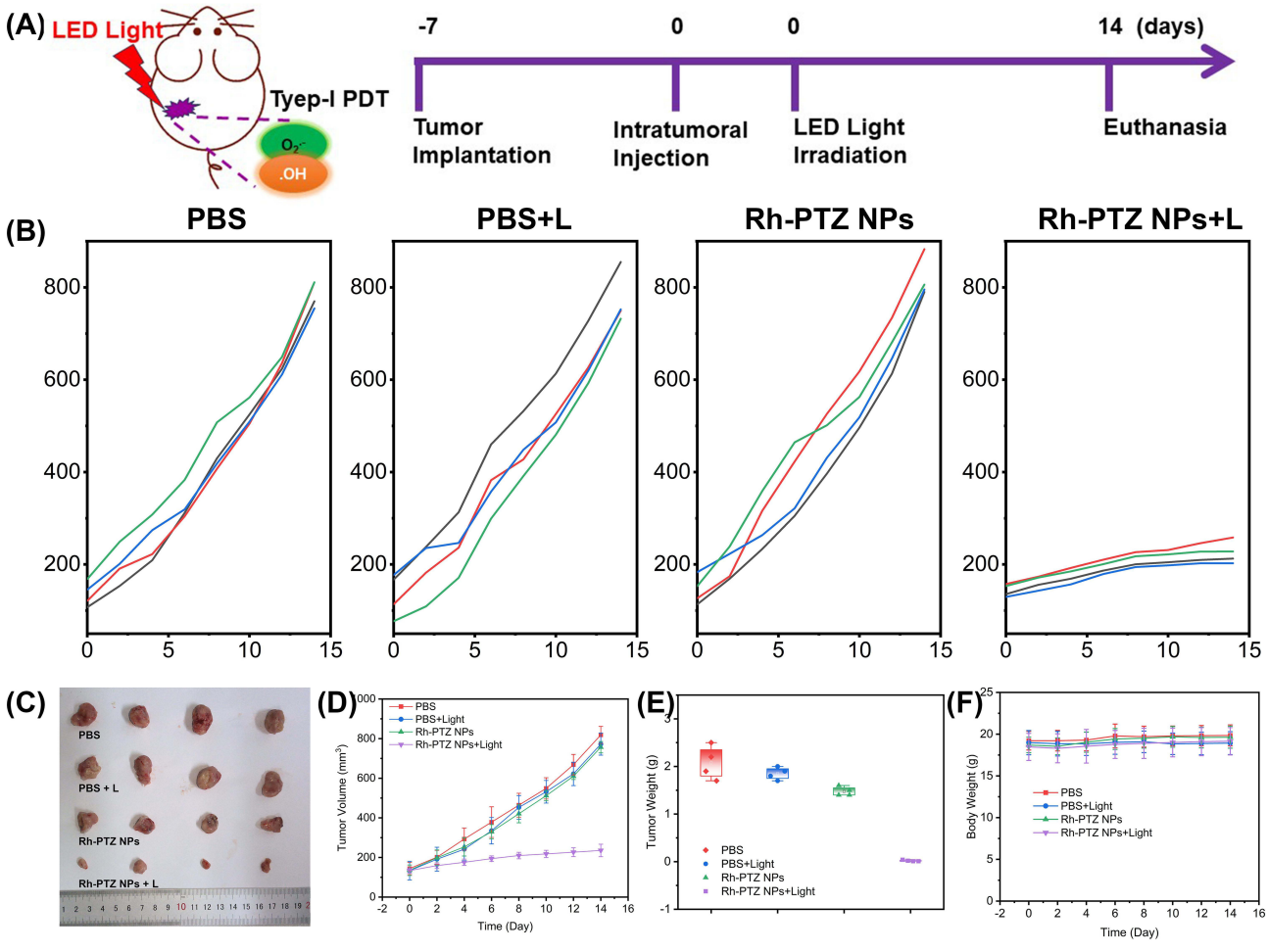

Figure 4 Anticancer activity of Rh-PTZ on mice bearing 4T1 orthotropic breast cancer. (**A**) Schematic illustration of treatment schedules. (**B**) Tumor volumes of different treatment groups. (**C**) Tumor growth inhibition curves. (**D**) Images of tumors excised on day 14 post-treatment. (**E**) Tumor weight of different treatment groups after 14 days. (**F**) The body weight of different treatment groups after 14 days.

cells compared to the Rh-PTZ +L group (Figure S19). Furthermore, the Rh-PTZ +L group demonstrated enhanced green fluorescence in TUNEL staining (Figure S20), suggesting augmented cell apoptosis and necrosis. All these results confirmed that the apoptosis and necrosis of tumor cells were detected in the 'Rh-PTZ + L' group, agreeing with the tumor inhibition effect.

The Mechanism of Anti-Tumor Effect

To further research the mechanisms of the excellent anti-tumor effects caused by the mitochondria-targeted photodynamic therapy, the immune responses after different treatments were studied. The tumors were extracted 2 days following the last treatment for additional flow cytometric evaluation. Interestingly, mitochondria-targeted photodynamic therapy (Rh-PTZ + L) would considerably boost the DCs maturation inside tumor tissues and emphasized the significance of mitochondria-targeted PDT to induce ICD, which encouraged DC maturation (Figure 5A).

CD8+ cytotoxic T lymphocytes (CTLs) are preferred immune cells for targeting malignancy. Infiltration of CD8+ T cells in tumors after different therapies was investigated to confirm the activation of immune response. The enhancement of CD8+ T cells in tumor tissues was found after mitochondria-targeting type-I PDT treatment (Figure 5B). The number of CD8+ T cells in Rh-PTZ +L group was 20.4%, which was r higher than that for other groups. These results indicated that mitochondria-targeting type I PDT treatment demonstrated the highest efficacy in the activation of immunological T cells.

Notably, a decrease in myeloid-derived suppressor cells (MDSCs), the immunosuppressive cells, was also found after mitochondria-targeting type-I PDT treatment (Figure 5C). The number of MDSCs cells in Rh-PTZ +L groups was 26.1%, which was around 0.67-fold lower than that for PBS and the other groups. These findings substantiate that Rh-PTZ + L could alleviate the immunosuppressive microenvironment.

Finally, the serum levels of immune-relevant inflammatory cytokines were evaluated. The level of tumor necrosis factor-alpha (TNF-α), interleukin 6 (IL-6), and interferon-gamma (IFN-γ) were dramatically increased in the Rh-PTZ + L group compared with other groups (Figure 5D–F). These in vivo data verified that the mitochondria-targeting photodynamic treatment may activate a robust immunological response.

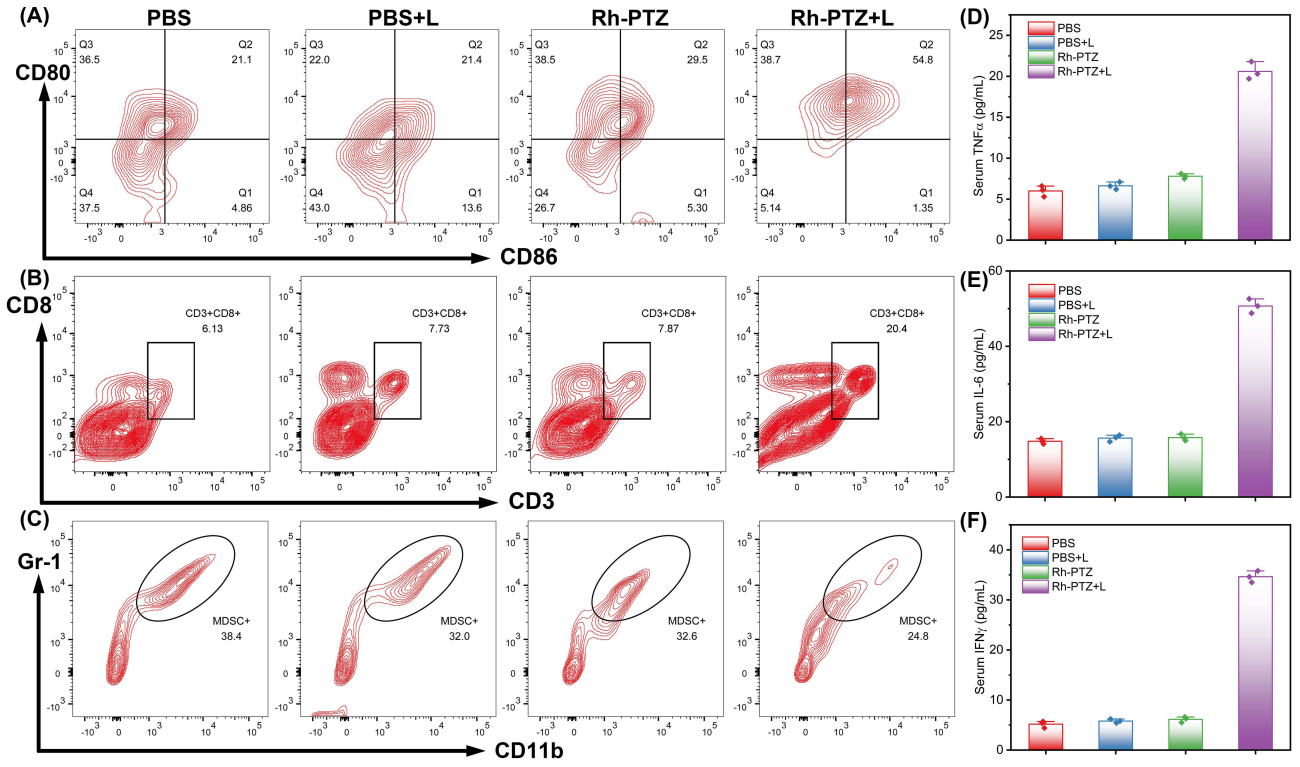

Figure 5 The mechanism of anti-tumor effect. (**A**)Flow cytometric plots of matured DCs in tumor tissues after treatments. (**B**) Flow cytometric plots of CD3+ CD8+ T cells in tumor tissues after treatments. (**C**) Flow cytometric plots of MDSC+ cells in tumor tissues after treatments. (D~F) TNF, IL-6, and IFN levels in serum after different treatments.

https://doi.org/10.2147/IJN.S494970

Biosafe

The biosafety of Rh-PTZ was ultimately assessed. Serum biochemistry studies were undertaken to investigate liver and renal function biomarker, such as creatinine (CRT), blood urea nitrogen (BUN), urea (UA), alanine transaminase (ALT), albumin (ALB), and aspartate transaminase (AST). All the parameters fall within the respective normal range (Figure S21), demonstrating the absence of liver or kidney dysfunction. Furthermore, healthy BALB/c mice received intravenous injections of Rh-PTZ on days 0, 3, 6, and 9. On day 16, the major organs (kidneys, spleen, heart, lung, and liver) were collected for H&E staining. The mice treated with Rh-PTZ demonstrated no discernible histological abnormalities in major organs (Figure S22). All these findings verified the high biocompatibility of Rh-PTZ.

Conclusion

In summary, this work provides a mitochondrial targeting type I photosensitizer based on phenothiazine (Rh-PTZ) for photoimmunotherapy of hypoxic tumors. Rh-PTZ could accurately target mitochondria, generate $O_2^{\bullet-}$ and •OH in situ, damage mitochondria, and induce intracellular oxidative stress. Subsequently, the mitochondria-targeted type-I PDT enhanced the ICD effect via mitochondrial stress, accelerated the maturation of DCs, promoted infiltration of CD8+ T cells, and alleviated immunosuppressive TME. In conclusion, our study provides a new type-I photosensitizer capable of accomplishing type-I photodynamic effect and mitochondrial stress-induced ICD, which may supply new approach for the development of cancer photoimmunotherapy.

Acknowledgments

This work was sponsored by the Natural Science Foundation of Guangdong Province, China (No. 2023A1515012934), Guangdong Province Marine Economic Development Project (GDNRC[2024]27), Plan on enhancing scientific research in GMU, and the Guangzhou Basic and Applied Basic Research Funds (No. SL2023A04J02451).

Disclosure

The authors report no conflicts of interest in this work.

References

1. Ahmed A, Tait SWG. Targeting immunogenic cell death in cancer. *Mol Oncol*. 2020;14(12):2994–3006. doi:10.1002/1878-0261.12851
2. Duan X, Chan C, Lin W. Nanoparticle-Mediated Immunogenic Cell Death Enables and Potentiates Cancer Immunotherapy. *Angew Chem Int Ed Engl*. 2019;58(3):670–680. doi:10.1002/anie.201804882
3. Kroemer G, Galassi C, Zitvogel L, Galluzzi L. Immunogenic cell stress and death. *Nat Immunol*. 2022;23(4):487–500. doi:10.1038/s41590-022-01132-2
4. Fan Z, Wu S, Deng H, Li G, Huang L, Liu H. Light-Triggered Nanozymes Remodel the Tumor Hypoxic and Immunosuppressive Microenvironment for Ferroptosis-Enhanced Antitumor Immunity. *ACS Nano*. 2024;18(19):12261–12275. doi:10.1021/acsnano.4c00844
5. Liu C, Wang Y, Li L, et al. Engineered extracellular vesicles and their mimetics for cancer immunotherapy. *J Control Release*. 2022;349:679–698. doi:10.1016/j.jconrel.2022.05.062
6. Fucikova J, Kepp O, Kasikova L, et al. Detection of immunogenic cell death and its relevance for cancer therapy. *Cell Death Dis*. 2020;11(11):1013. doi:10.1038/s41419-020-03221-2
7. Li Z, Lai X, Fu S, et al. Immunogenic Cell Death Activates the Tumor Immune Microenvironment to Boost the Immunotherapy Efficiency. *Adv Sci*. 2022;9(22):e2201734. doi:10.1002/advs.202201734
8. Alzeibak R, Mishchenko TA, Shilyagina NY, Balalaeva VMV IV, Krysko DV. Targeting immunogenic cancer cell death by photodynamic therapy: past, present and future. *J Immunother Cancer*. 2021;9(1). doi:10.1136/jitc-2020-001926
9. Cui X, Li X, Peng C, et al. Beyond External Light: on-Spot Light Generation or Light Delivery for Highly Penetrated Photodynamic Therapy. *ACS Nano*. 2023;17(21):20776–20803. doi:10.1021/acsnano.3c05619
10. Li W, Yang J, Luo L, et al. Targeting photodynamic and photothermal therapy to the endoplasmic reticulum enhances immunogenic cancer cell death. *Nat Commun*. 2019;10(1):3349. doi:10.1038/s41467-019-11269-8
11. Li Z, Zhou Z, Wang Y, et al. Activatable nano-photosensitizers for precise photodynamic cancer therapy. *Coord Chem Rev*. 2023;493:215324. doi:10.1016/j.ccr.2023.215324
12. Zhang S, Wang J, Kong Z, et al. Emerging photodynamic nanotherapeutics for inducing immunogenic cell death and potentiating cancer immunotherapy. *Biomaterials*. 2022;282:121433. doi:10.1016/j.biomaterials.2022.121433
13. Lin Q, Wang Y, Wang L, Fan Z. Engineered macrophage-derived cellular vesicles for NIR-II fluorescence imaging-guided precise cancer photoimmunotherapy. *Colloids Surf B Biointerfaces*. 2024;235:113770. doi:10.1016/j.colsurfb.2024.113770
14. Chen J, Fan T, Xie Z, et al. Advances in nanomaterials for photodynamic therapy applications: status and challenges. *Biomaterials*. 2020;237:119827. doi:10.1016/j.biomaterials.2020.119827
15. Lucky SS, Soo KC, Zhang Y. Nanoparticles in photodynamic therapy. *Chem Rev*. 2015;115(4):1990–2042. doi:10.1021/cr5004198

16. Zhao X, Liu J, Fan J, Chao H, Peng X. Recent progress in photosensitizers for overcoming the challenges of photodynamic therapy: from molecular design to application. *Chem Soc Rev*. 2021;50(6):4185–4219. doi:10.1039/d0cs00173b
17. Chen W, Wang Z, Hong G, Du J, Song F, Peng X. Self-assembly-integrated tumor targeting and electron transfer programming towards boosting tumor type I photodynamic therapy. *Chem Sci*. 2024;15(28):10945–10953. doi:10.1039/d4sc03008g
18. Zhuang J, Wang B, Chen H, et al. Efficient NIR-II Type-I AIE Photosensitizer for Mitochondria-Targeted Photodynamic Therapy through Synergistic Apoptosis–Ferroptosis. *ACS Nano*. 2023;17(10):9110–9125. doi:10.1021/acsnano.2c12319
19. Zou J, Li Z, Zhu Y, et al. pH/GSH dual responsive nanosystem for nitric oxide generation enhanced type I photodynamic therapy. *Bioact. Mater.* 2024;34:414–421. doi:10.1016/j.bioactmat.2023.12.023
20. Kalyuzhny G, Murray RW. Ligand effects on optical properties of CdSe nanocrystals. *J Phys Chem B*. 2005;109(15):7012–7021. doi:10.1021/jp045352x
21. Moan J, Berg K. The photodegradation of porphyrins in cells can be used to estimate the lifetime of singlet oxygen. *Photochem Photobiol*. 1991;53(4):549–553. doi:10.1111/j.1751-1097.1991.tb03669.x
22. Jin T, Wang C, Tian Y, Dai C, Zhu Y, Xu F. Mitochondrial metabolic reprogramming: an important player in liver cancer progression. *Cancer Lett*. 2020;470:197–203. doi:10.1016/j.canlet.2019.11.029
23. Nunnari J, Suomalainen A. Mitochondria: in sickness and in health. *Cell*. 2012;148(6):1145–1159. doi:10.1016/j.cell.2012.02.035
24. Tan YQ, Zhang X, Zhang S, et al. Mitochondria: the metabolic switch of cellular oncogenic transformation. *Biochim Biophys Acta Rev Cancer*. 2021;1876(1):188534. doi:10.1016/j.bbcan.2021.188534
25. Zong WX, Rabinowitz JD, White E. Mitochondria and Cancer. *Mol Cell*. 2016;61(5):667–676. doi:10.1016/j.molcel.2016.02.011
26. Bai X, Lin Y, Gong L, et al. Nanoparticles that target the mitochondria of tumor cells to restore oxygen supply for photodynamic therapy: design and preclinical validation against breast cancer. *J Control Release*. 2023;362:356–370. doi:10.1016/j.jconrel.2023.07.064
27. Li Y, Yang J, Chen X, et al. Mitochondrial-targeting and NIR-responsive Mn3O4@PDA@Pd-SS31 nanozymes reduce oxidative stress and reverse mitochondrial dysfunction to alleviate osteoarthritis. *Biomaterials*. 2024:305,122449. doi:10.1016/j.biomaterials.2023.122449
28. Wang SZ, Guo Y, Zhang X, et al. Mitochondria-Targeted Photodynamic and Mild-Temperature Photothermal Therapy for Realizing Enhanced Immunogenic Cancer Cell Death via Mitochondrial Stress. *Adv Funct Mater*. 2023;33(42):e202303328. doi:10.1002/adfm.202303328
29. Zhang J, Gao B, Ye B, et al. Mitochondrial-Targeted Delivery of Polyphenol-Mediated Antioxidases Complexes against Pyroptosis and Inflammatory Diseases. *Adv Mater*. 2023;35(11):e2208571. doi:10.1002/adma.202208571
30. Liu P, Ren F, Son S, et al. Mitochondrial targeted AIEgen phototheranostics for bypassing immune barrier via encumbering mitochondria functions. *Biomaterials*. 2022;283:121409. doi:10.1016/j.biomaterials.2022.121409
31. Wang Y, Wang W, Gu R, et al. In Situ Vaccination with Mitochondria-Targeting Immunogenic Death Inducer Elicits CD8(+) T Cell-Dependent Antitumor Immunity to Boost Tumor Immunotherapy. *Adv Sci*. 2023;10(20):e2300286. doi:10.1002/advs.202300286
32. Lin R, Liu J, Xu W, et al. Type I Photosensitization with Strong Hydroxyl Radical Generation in NIR Dye Boosted by Vigorous Intramolecular Motions for Synergistic Therapy. *Adv Mater*. 2023;35(33):2303212. doi:10.1002/adma.202303212
33. Sun J, Cai X, Wang C, et al. Cascade Reactions by Nitric Oxide and Hydrogen Radical for Anti-Hypoxia Photodynamic Therapy Using an Activatable Photosensitizer. *J Am Chem Soc*. 2021;143(2):868–878. doi:10.1021/jacs.0c10517
34. Tang X, Chen L, Wang Y, et al. Multimodal phototherapy agents target lipid droplets for near-infrared imaging-guided type I photodynamic/photothermal therapy. *Acta Biomater*. 2024;180:394–406. doi:10.1016/j.actbio.2024.04.014
35. Zhang L, Yu Y, Ding K, et al. Tumor microenvironment ameliorative and adaptive nanoparticles with photothermal-to-photodynamic switch for cancer phototherapy. *Biomaterials*. 2025;313:122771. doi:10.1016/j.biomaterials.2024.122771
36. Zhang T, Zhang J, Wang F-B, et al. Mitochondria-Targeting Phototheranostics by Aggregation-Induced NIR-II Emission Luminogens: modulating Intramolecular Motion by Electron Acceptor Engineering for Multi-Modal Synergistic Therapy. *Adv Funct Mater*. 2022;32(16):2110526. doi:10.1002/adfm.202110526
37. Tu Y, Xia W, Wu X, Wang L. A lysosome-targeted near-infrared photosensitizer for photodynamic therapy and two-photon fluorescence imaging. *Org Biomol Chem*. 2021;19(27):6098–6107. doi:10.1039/d1ob00684c
38. Zhou Y, Zhang D, He G, et al. A lysosomal targeted NIR photosensitizer for photodynamic therapy and two-photon fluorescence imaging. *J Mater Chem B*. 2021;9(4):1009–1017. doi:10.1039/d0tb02692a
39. Zhang D, Yang J, Liu C, Ye S, Zhang Q, Liu R. An Acceptor-π-Donor Structured Organic Chromophore for NIR Triggered Thermal Ablation of Tumor via DNA Damage-Mediated Apoptosis. *Int J Nanomed*. 2021;16:4901–4911. doi:10.2147/ijn.S319089
40. Kenry CC, Liu B. Enhancing the performance of pure organic room-temperature phosphorescent luminophores. *Nat Commun*. 2019;10(1):2111. doi:10.1038/s41467-019-10033-2